

The structure of radiative shock waves

I. The method of global iterations

Yu. A. Fadeyev¹ and D. Gillet²

¹ Institute for Astronomy of the Russian Academy of Sciences, Pyatnitskaya 48, 109017 Moscow, Russia (fadeyev@inasan.rssi.ru)

² Observatoire de Haute-Provence - CNRS, F-04870 Saint-Michel l'Observatoire, France (gillet@obs-hp.fr)

Received 4 August 1997 / Accepted 2 January 1998

Abstract. The structure of steady plane-parallel radiative shock waves propagating through the hydrogen gas undergoing partial ionization and excitation of bound atomic states is investigated in terms of the self-consistent solution of the equations of fluid dynamics, radiation transfer and atomic kinetics. The shock wave model is represented by a flat finite slab with no incoming radiation from external sources at both its boundaries. The self-consistent solution is obtained using the global iteration procedure each step of which involves (1) integration of the fluid dynamics and rate equations for the preshock and postshock regions, consecutively, both solutions being fitted by the Rankine-Hugoniot relations at the discontinuous jump; (2) solution of the radiation transfer equation for the whole slab. The global iteration procedure is shown to converge to the stable solution which allows for the strong coupling of the gas flow and the radiation field produced by this flow. Application of the method is demonstrated for the shock waves with upstream velocities of $15 \text{ Km s}^{-1} \leq U_1 \leq 60 \text{ Km s}^{-1}$ (i.e. with upstream Mach numbers $2.3 \leq M_1 \leq 9.3$) and the hydrogen gas of unperturbed temperature $T = 3000\text{K}$ and density $\rho = 10^{-10} \text{ gm cm}^{-3}$.

Key words: shock waves – hydrodynamics – radiative transfer – stars: atmospheres

1. Introduction

Radiative shock waves belong to the conspicuous phenomena demonstrating the tight interplay between hydrodynamic motions and the radiation field. The role of this interplay is strongest in the low gas density flows, so the shocks are of tremendous importance in astrophysics. They are observed in a wide variety of astrophysical phenomena: nova and supernova explosions, bright filaments in old supernova remnants, accretion flows in protostellar clouds. Shock waves are detected also in atmospheres of radially pulsating variables such as Cepheids, RR Lyr, W Vir, RV Tau and Mira type stars. Periodic shocks propagating through pulsating atmospheres lead to the distention of outer atmospheric layers and to the mass loss.

Importance of radiative shock waves attracted attention of many authors but nevertheless the shock properties are explained quite well still qualitatively (see, for example, Zel'dovich & Raizer 1966; Skalafuris 1968; Mihalas & Mihalas 1984; Liberman & Velikovich 1986). The principal difficulty in obtaining the correct quantitative description of the shock wave structure is that the model has to allow for the strong coupling between the gas flow and the radiation field, both them being characterized by substantial departures from LTE. Solution of this problem encounters serious difficulties, so that in immensely numerous studies available at present in the literature the authors used various assumptions and simplifications (e.g. local thermodynamic equilibrium, treatment of the radiation transfer in diffusion approximation, neglecting the opacity in the Balmer continuum etc.). Many of these assumptions were found later inadequate or leading to uncertain conclusions. For instance, Kogure (1962), Sachdev (1968) and Hill (1972) used the LTE approximation which does not hold as emphasized later Narita (1973). Considering the hydrogen gas, Whitney & Skalafuris (1963) relaxed this assumption but incorrectly assumed that the postshock region is transparent for all hydrogen continua. Finally, Narita (1973) took into account the opacity in the both Lyman and Balmer continua. The most elaborate numerical modelling of radiative shock waves based on the self-consistent solution of the equations of fluid dynamics, radiative transfer and atomic level populations was done by Klein et al. (1976, 1978). However, the coarse zoning ($\sim 10^6 \text{ cm}$) did not allow to authors to consider the detailed structure of the shock front including the radiative precursor and the thermalization zone where the electron temperature gradually equalizes with temperature of heavy particles. Nevertheless, this approach was found to be enough for consideration of shock dynamics in atmospheres of A-type stars because the radiative precursor is not so important due to the high temperature of the unperturbed gas.

Because astrophysical shocks in stellar atmospheres propagate through the partially ionized hydrogen gas, a substantial fraction of photons produced within the wake are absorbed in the radiative precursor. As was shown by Gillet & Lafon (1984, 1990) the structure of the radiative precursor is complex and should be treated with same degree of approximation as the postshock region. In their studies Gillet & Lafon (1984, 1990)

treated the radiative transfer as an initial value problem which was solved using the shooting method. The principal obstacle in such an approach is that the transfer equation possesses a singularity in the postshock region (Gillet et al. 1989). Indeed, application of the eigenvalue methods for solution of the nongrey transfer problem is affected by exponentially growing errors (Mihalas 1978).

One of the first attempts to obtain the self-consistent solution for the shock wave structure was undertaken by Nelson & Goulard (1969) and Nelson (1973). They considered the shock waves propagating through the argon-like gas with upstream Mach numbers of $M_1 = 18$ and $M_1 = 24$. The continuity, momentum and energy equations were written in the integral representation whereas the radiation transfer was treated in the simplified formulation. The studies of radiative shock waves in helium and nitrogen done by Clarke & Ferrari (1965), Farnsworth & Clarke (1971) and Foley & Clarke (1973) seem to be the best among known in the literature. The authors emphasized the crucial role of the radiation transfer treatment and employed the formal solution of the transfer equation. The self-consistent shock wave models were obtained in these studies with iteration procedure. Unfortunately, there is a problem of exponential factors when the formal solution is applied for optically thick layers.

In this paper we present a new approach based on the iterative solution of the equations of fluid dynamics, the rate equations and the radiation transfer equation. The momentum equation, the energy and rate equations are written in the form of ordinary differential equations. These equations are stiff and such a representation is most appropriate from the point of view of stability and small truncation errors. The radiation transfer is treated as a two-point boundary value problem. This allows us to obtain the stable solution of the transfer equation for the whole spectral range including both the opaque Lyman continuum and the more transparent higher order continua. The method of global iterations takes into account the coupling between the gas flow and the radiation field, so that the structure of the radiative shock wave is considered in terms of the self-consistent model.

In the framework of this first approach, only devoted to provide a new technique for obtaining the self-consistent solution, we consider the structure of steady, plane-parallel shock waves propagating through an infinite, isotropic, pure hydrogen plasma. The steady assumption is correct, for example, to a good degree of approximation in most applications to stellar atmospheres. Indeed, the time required for the gas flow to cross the shock wake with typical thickness of 10^4 - 10^7 cm is much less than the characteristic time during of which the shock wave energy appreciably decreases. In pulsating stars, the radiative lifetime of a shock is between a few hours and a few months, which, consequently, is much larger than the 10^{-2} - 10 s of the gas flow time to cross the shock wake. Accuracy of the plane-parallel approximation follows from the very small width of the shock wave in comparison with stellar radius.

After describing the shock wave model (Sect. 2) we derive the system of ordinary differential equations (Sect. 3). The

radiation transfer equation is solved for the whole shock wave model using the Feautrier technique (Sect. 4). In Sect. 5 we show that the global iteration procedure comprising the initial value problem for ordinary differential equations and the two-point boundary value problem for radiation transfer converges to the self-consistent solution. Results of calculations demonstrating the applicability of the method are given in Sect. 6. Finally, in Sect. 7, we give some concluding remarks and discuss the future aspects of the problem.

2. The shock wave model

Consider a steady, plane-parallel shock wave propagating through the homogeneous medium which is at rest and consists of a pure hydrogen gas. No radiation and gravitational forces from external sources are assumed to be present. The problem to be solved is that to describe the spatial structure of the shock wave in terms of the self-consistent solution of the equations of fluid dynamics, the rate equations for hydrogen atomic level populations and the radiation transfer equation. The problem is characterized by three input parameters: the temperature T_1 and the density ρ_1 of the unperturbed gas as well as the speed U_1 at which the gas material flows into the shock.

The structure of radiative shock waves is schematically divided into four zones: (1) a precursor, where the gas is heated and is partially ionized by radiation emerging from the postshock region; (2) a very narrow zone, where a major part of the kinetic energy of the upstream flow is converted due to viscosity and conductivity into the thermal energy of translational motions of heavy particles, that is, neutral atoms and ions; (3) a thermalization zone, where the kinetic energy of translational motions of heavy particles is redistributed among various degrees of freedom; (4) a radiative relaxation zone, where hydrogen atoms recombine and the gas radiatively cools. Because of its extremely small width (a few mean free paths of gas particles), the second zone cannot be correctly described in terms of the fluid dynamics and, hence, should be considered as a discontinuous jump across which the Rankine-Hugoniot equations are applied. Thus, the present study is confined by consideration of the spatial structure of the radiative precursor as well as the thermalization and relaxation zones.

Let the origin of the comoving frame to coincide with infinitesimally thin discontinuous jump dividing the medium into the preshock and the postshock regions. The spatial coordinate is $X = 0$ at the discontinuous jump, is negative in the preshock region and is positive in the postshock region. The shock wave model is represented by a flat finite slab comoving with discontinuous jump. Thus, the velocity of the gas material flowing through the slab is always positive: $U = dX/dt > 0$. At the outer boundary of the preshock region with spatial coordinate $X_1 < 0$ the gas is assumed to be unperturbed. The spatial coordinate of the postshock outer boundary is $X_N > 0$ and physical properties of the gas at this point are not known.

The radiation transfer equation is solved for the whole slab in the framework of the two-point boundary value problem, therefore the slab is represented by a set of spatial cells. The dis-

continuous jump locates at the J -th cell boundary with spatial coordinate $X_J = 0$. The cells are inequally spaced, are smallest at the discontinuous jump and increase outwardly in both directions from the discontinuous jump according to the geometrical progression. Following the traditional conventions of computational radiation hydrodynamics (see, for example, Mihalas & Mihalas 1984), all thermodynamic variables are defined at the cell centers $X_{j-1/2} = \frac{1}{2}(X_{j-1} + X_j)$ and are denoted by half-integer subscripts. The spatial coordinates of the cell centers nearest to the discontinuous jump hereafter are referred as the inner boundaries of the preshock and postshock regions, respectively, and are denoted as $X_{J-1/2}$ and $X_{J+1/2}$.

The assumption of the steady shock wave allows us to reduce the equations of fluid dynamics to a system of ordinary differential equations. In order to take into account the coupling between hydrodynamic motions and the radiation field we employ the iteration procedure comprising the consecutive solution of the transfer equation and integration of the rate and fluid dynamics equations. The starting point for integration of ordinary differential equations is the outer boundary of the preshock region X_1 where the gas is assumed to be unperturbed. The preshock integration is done within the interval $[X_1, X_{J-1/2}]$. Then we solve the Rankine-Hugoniot equations

$$\rho U \equiv \dot{m} = \mathbf{C}_0, \quad (1)$$

$$\dot{m}U + P_g = \mathbf{C}_1, \quad (2)$$

$$\dot{m} \left(\frac{h}{\rho} + \frac{1}{2}U^2 \right) + F_r = \mathbf{C}_2, \quad (3)$$

where h is the enthalpy,

$$h = 5/3E_{trans} + E_{rot} + E_{vib} + E_{el} + E_{diss} + E_{ion} \quad (4)$$

where E_{trans} , E_{rot} , E_{vib} , E_{el} , E_{diss} and E_{ion} are the translational energy; rotational, vibrational, electronic excitation internal energies and dissociation and ionization potential energies respectively. In this paper only E_{trans} and E_{ion} are different of zero. F_r is the total radiative flux, \mathbf{C}_0 , \mathbf{C}_1 and \mathbf{C}_2 are the mass, momentum and energy fluxes across the discontinuous jump. In the present study we assume that the radiation pressure P_r and the radiation energy density E_{rad} can be neglected in comparison with gas pressure and internal energy of the gas material. Applicability of this assumption is shown below.

Let us designate, for the sake of convenience, the quantities defined at $X_{J-1/2}$ by the superscript minus and the quantities defined at $X_{J+1/2}$ by the superscript plus. Eqs. (1) – (3) are solved for the temperature of heavy particles T_a^+ and the inverse compression ratio $\omega = \rho^-/\rho^+ = U^+/U^-$. Assuming that hydrogen atoms undergo across the discontinuous jump neither excitation of the bound levels nor ionization and that the hydrogen ions have the same temperature as that of neutral hydrogen atoms, we obtain

$$T_a^+ = T_a^- + \frac{n_e^-}{n_H^-} (T_e^- - T_e^+) + \frac{1}{5} \frac{\dot{m}U^-}{n_H^- k} (1 - \omega^2) + \frac{2}{5} \frac{F_r^- - F_r^+}{U^- n_H^- k}, \quad (5)$$

where k is the Boltzmann constant, n_H and n_e are the total numbers of hydrogen atoms and free electrons per unit volume, respectively. It should be noted that jump conditions (1) – (3) are not applied to the infinitesimally thin discontinuous jump coinciding with the cell interface X_J but rather relate the physical variables at cell centers $X_{J-1/2}$ and $X_{J+1/2}$. That is why the term containing $F_r^- - F_r^+$ into Eq. (5) does not cancel and has to be taken into account. The inverse compression ratio is obtained from

$$A\omega^2 + B\omega + C = 0, \quad (6)$$

where

$$A = \frac{4}{5} \dot{m}U^-, \quad (7)$$

$$B = -\dot{m}U^- - P_g^-, \quad (8)$$

$$C = \frac{1}{5} \dot{m}U^- + P_g^- + \frac{2}{5} \frac{F_r^- - F_r^+}{U^-}. \quad (9)$$

Eqs. (5) and (6) imply that the postshock electron temperature T_e^+ at the cell center $X_{J+1/2}$ is known. Across the discontinuous jump the electron gas undergoes the adiabatic compression and the electron temperature increases by a factor of $1/\omega^{\gamma-1}$, where γ is the ratio of specific heats (Zel'dovich & Raizer 1966). Because the adiabatic compression has a weak effect and the electron heat conduction is out the scope of the present study, we assumed that the electron temperature does not change across the discontinuous jump, that is, $T_e^- = T_e^+$.

Eqs. (5) and (6) are solved to determine the initial conditions for the postshock integration which is done within the interval $[X_{J+1/2}, X_N]$. Integration of ordinary differential equations provides with spatial distributions of electron temperature T_e , gas density ρ , the number densities of free electrons n_e and atomic level populations Ξ . These quantities are used in solution of the radiation transfer equation which gives improved radiation intensities within the whole slab. The global iteration procedure consisting of the integration of ordinary differential equations and solution of the radiation transfer equation continues until the relative changes of all quantities become less than the convergence criterion. Below we discuss details of the global iteration procedure.

3. The system of ordinary differential equations

The solution vector to be found from integration of the system of ordinary differential equations consists of $L + 4$ variables and is

$$\mathbf{Y} = \{U, E'_a, E'_e, n'_e, n'_1, \dots, n'_L\}, \quad (10)$$

where L is the number of bound atomic states treated in non-LTE, U is the gas material velocity with respect to the discontinuous jump,

$$E'_a \equiv \frac{E_a}{\rho} = \frac{3}{2} \frac{n_H k T_a}{\rho} \quad (11)$$

is the specific translational kinetic energy of heavy particles (neutral atoms and ions),

$$E'_e \equiv \frac{E_e}{\rho} = \frac{3 n_e k T_e}{2 \rho} \quad (12)$$

is the specific translational kinetic energy of free electrons, n'_e is the number of free electrons per unit mass, ϑ' is the number of hydrogen atoms in the i -th state per unit mass. Hereafter the prime implies that the quantity is expressed per unit mass. The solution vector \mathbf{Y} does not contain the gas density ρ because this variable can be easily evaluated from the mass conservation relation (1).

Thus, the system of ordinary differential equations consists of the momentum equation, two energy equations for heavy particles and free electrons, the rate equation for free electrons and L rate equations for non-LTE bound states of the hydrogen atom:

$$\frac{dU}{dt} = -\frac{1}{\rho} \frac{dP_g}{dX}, \quad (13)$$

$$\frac{dE'_a}{dt} = -P_a \frac{dV}{dt} - Q_{\text{elc}}, \quad (14)$$

$$\frac{dE'_e}{dt} = -P_e \frac{dV}{dt} + Q_{\text{elc}} + Q_{\text{inc}}, \quad (15)$$

$$\frac{dn'_e}{dt} = \frac{1}{\rho} \sum_{i=1}^L (\vartheta P_{ik} - n_e P_{ki}), \quad (16)$$

$$\frac{d\vartheta'}{dt} = \frac{1}{\rho} (n_e P_{ki} - \vartheta P_{ik}), \quad (i = 1, \dots, L), \quad (17)$$

where $P_a = n_H k T_a$ is the partial pressure of heavy particles, $P_e = n_e k T_e$ is the electron pressure, Q_{elc} and Q_{inc} are the rates of energy gain by electrons in elastic and inelastic collisions, respectively, P_{ik} and P_{ki} are the total, that is collisional plus radiative, ionization and recombination rates, respectively. It should be noted that in the present study we consider only bound-free transitions, so that Eqs. (16) and (17) contain only ionization and recombination terms.

The system of ordinary differential equations (13) – (17) written in the form of derivatives with respect to time t is not appropriate for calculation of the spatial structure, so that these equations should be rewritten in order their left-hand sides are replaced by derivatives with respect to the spatial coordinate X . Furthermore, the space derivative of the gas pressure P_g in Eq. (13) and the time derivative of the specific volume V in Eqs. (14) and (15) have to be expressed in terms of integrated variables. To this end we write the gas pressure as a sum of translational kinetic energies:

$$P_g = n_H k T_a + n_e k T_e = \frac{2}{3} E_a + \frac{2}{3} E_e, \quad (18)$$

whereas the time derivative of the specific volume is determined from Eq. (2):

$$\frac{dV}{dt} = -\frac{1}{\dot{m}^2} \frac{dP_g}{dt}. \quad (19)$$

Expressing the time derivative of the specific volume in terms of the gas pressure according to Eq. (19), P_g according to Eq. (18)

in terms of integrated quantities E'_a and E'_e and substituting Eqs. (18) and (19) into Eqs. (13) – (17), we obtain the following system of ordinary differential equations with right-hand sides depending only on the independent variable X and integrated variables $\{U, E'_a, E'_e, n'_e, n'_1, \dots, n'_L\}$:

$$\frac{dU}{dX} = -\frac{\dot{A}}{U} (\mathcal{B}_a + \mathcal{B}_e), \quad (20)$$

$$\frac{dE'_a}{dX} = \mathcal{B}_a (1 - \mathcal{C}_e) + \mathcal{B}_e \mathcal{C}_a, \quad (21)$$

$$\frac{dE'_e}{dX} = \mathcal{B}_a \mathcal{C}_e + \mathcal{B}_e (1 - \mathcal{C}_a), \quad (22)$$

$$\frac{dn'_e}{dX} = \sum_{i=1}^L \frac{\vartheta P_{ik} - n_e P_{ki}}{\dot{m}}, \quad (23)$$

$$\frac{d\vartheta'}{dX} = \frac{n_e P_{ki} - \vartheta P_{ik}}{\dot{m}}, \quad (i = 1, \dots, L), \quad (24)$$

where

$$\dot{A} = \frac{2}{3} \frac{U^2}{U^2 - a_T^2}, \quad (25)$$

$$\mathcal{B}_a = -\frac{Q_{\text{elc}}}{U} \frac{1 - \beta^2}{1 - \frac{5}{3}\beta^2}, \quad (26)$$

$$\mathcal{B}_e = \left\{ \frac{Q_{\text{elc}}}{U} - \chi_H \left[\frac{dn'_e}{dX} + \sum_{i=1}^L \left(1 - \frac{1}{i^2} \right) \frac{d\vartheta'}{dX} \right] - \frac{\nabla \cdot \mathbf{F}_r}{\dot{m}} \right\} \frac{1 - \beta^2}{1 - \frac{5}{3}\beta^2}, \quad (27)$$

$$\mathcal{C}_a = \frac{\dot{A} P_a}{U \dot{m}}, \quad (28)$$

$$\mathcal{C}_e = \frac{\dot{A} P_e}{U \dot{m}}, \quad (29)$$

$\beta = a_T/U$, $a_T = \sqrt{P_g/\rho}$ is isothermal sound speed, $\chi_H = 13.598$ eV is the ionization potential of the hydrogen atom.

In obtaining Eq. (27) we expressed the rate of energy gain by electrons in inelastic collisions as (Murty 1971)

$$Q_{\text{inc}} = -\frac{d}{dt} (E'_I + E'_{\text{ex}}) - \nabla \cdot \mathbf{F}_r, \quad (30)$$

where E'_I and E'_{ex} are ionization and excitation energies per unit mass,

$$\nabla \cdot \mathbf{F}_r = 4\pi \int_0^\infty (\eta_\nu - \kappa_\nu J_\nu) d\nu \quad (31)$$

is the divergence of radiative flux, J_ν is the mean intensity of radiation, η_ν and κ_ν are the total emission and absorption coefficients.

Free electrons acquire the energy from heavy particles in elastic collisions with hydrogen ions and neutral hydrogen atoms, hence,

$$Q_{\text{elc}} = Q_{\text{ei}} + Q_{\text{ea}}, \quad (32)$$

where Q_{ei} and Q_{ea} are the corresponding rates of energy gain. The rate of energy gain by electrons in elastic collisions with hydrogen ions per unit mass is (Spitzer & Härm 1953)

$$Q_{ei} = \frac{2}{3} \frac{n_e}{\rho} k \frac{T_a - T_e}{t_{eq}}, \quad (33)$$

where t_{eq} is the time of equipartition given by

$$t_{eq} = \frac{252 T_e^{3/2}}{n_e \ln \Lambda} \quad (34)$$

and

$$\ln \Lambda = 9.43 + 1.15 \log (T_e^3 / n_e). \quad (35)$$

The rate of energy gain by electrons in elastic collisions with neutral hydrogen atoms per unit mass is

$$Q_{ea} = \frac{n_e m_e}{n_H m_H} \frac{T_a - T_e}{T_e} n_1 \langle \sigma_{ea} v^3 \rangle, \quad (36)$$

where m_e and m_H are the mass of electron and the mass of hydrogen atom, respectively, and the elastic scattering cross section is (Narita 1973)

$$\begin{aligned} \langle \sigma_{ea} v^3 \rangle &= \int_0^\infty \sigma_{ea} v^3 f(v) dv = \\ &= 4\pi a_0^2 \left(\frac{8}{\pi}\right)^{1/2} \left(\frac{kT_e}{m_e}\right)^{3/2} \left[4 + \frac{24}{(1 + 2 \cdot 10^{-5} T_e)^3}\right]. \end{aligned} \quad (37)$$

Here a_0 is the Bohr radius.

Rate equations (23) and (24) imply that the number density of free electrons n_e and atomic level populations Ξ change due to bound-free transitions, that is, due to ionizations and recombinations. The total ionization rate is

$$P_{ik} = n_e C_{ik} + R_{ik}, \quad (38)$$

where the rate of collisional ionizations is given by

$$C_{ik} = \pi a_0^2 \left(\frac{8k}{m_e \pi}\right)^{1/2} T_e^{1/2} \exp\left(-\frac{\chi_i}{kT_e}\right) \Gamma_i(T_e), \quad (39)$$

$\chi_i = \chi_H / i^2$ is energy of ionization from the i -th level, $\Gamma_i(T)$ is a slowly varying function of T evaluated with approximation formulae by Mihalas (1967).

The rate of photoionizations is

$$R_{ik} = 4\pi \int_{\nu_{0i}}^\infty \frac{\alpha_{bf}}{h\nu} J_\nu d\nu, \quad (40)$$

where α_{bf} is an absorption cross-section at frequency ν in bound-free transition from the i -th state and ν_{0i} is a threshold frequency for ionization from the i -th state.

The total recombination rate is

$$P_{ki} = n_e C_{ki} + R_{ki}, \quad (41)$$

where the collisional recombination rate is given by

$$C_{ki} = \frac{\Xi^*}{n_e^*} C_{ik}. \quad (42)$$

The radiative recombination rate is

$$R_{ki} = \frac{\Xi^*}{n_e^*} R_{ik}^\dagger, \quad (43)$$

where

$$R_{ik}^\dagger = 4\pi \int_{\nu_{0i}}^\infty \frac{\alpha_{bf}}{h\nu} \exp\left(-\frac{h\nu}{kT_e}\right) \left(\frac{2h\nu^3}{c^2} + J_\nu\right) d\nu. \quad (44)$$

Substituting Eqs. (42) and (43) into Eq. (41) we obtain that the total recombination rate is

$$P_{ki} = \frac{\Xi^*}{n_e^*} \left(n_e C_{ik} + R_{ik}^\dagger\right). \quad (45)$$

The system of ordinary differential equations (20) – (24) is stiff because it is characterized by very different time constants due to the rate equations (23) and (24). In order to obtain the stable and enough correct solution of Eqs. (20) – (24) we used the Livermore solver for ordinary differential equations based on the GEAR package (Hindmarsh 1979).

4. The radiation transfer equation

For the shock wave models considered in the present study the extinction coefficient is highest at the Lyman edge frequency ν_{01} . In the preshock region the corresponding extinction coefficient is $\chi(\nu_{01}) \sim 3 \cdot 10^{-4} \text{ cm}^{-1}$. Behind the discontinuous jump the extinction coefficient initially decreases because of ionization of hydrogen atoms and then increases within the recombination zone. For all the models considered $\chi(\nu_{01}) \lesssim 5 \cdot 10^{-3} \text{ cm}^{-1}$. Thus, the time needed for photons to travel a mean free path is $t_{ph} = [c\chi(\nu_{01})]^{-1} \sim 7 \cdot 10^{-9} \text{ s}$, where c is the velocity of light. Because a characteristic structural length for Lyman photons is only a few mean free paths, a photon flight time is much shorter than the characteristic time of producing the changes due to hydrodynamic motions and, therefore, the time-derivative term in the transfer equation can be omitted because the radiation field is quasi static to a good accuracy.

In plane-parallel geometry the quasi static radiative transfer equation is written as

$$\mu \frac{dI_\nu}{d\tau_\nu} = I_\nu - S_\nu, \quad (46)$$

where I_ν is the specific intensity of radiation depending on the frequency ν , the directional cosine μ and the monochromatic optical depth $d\tau_\nu = \chi_\nu dX$.

The present study is confined by treatment of the continuum radiation transfer with total extinction coefficient given by

$$\chi_\nu = \kappa_{bf}(\nu) + \kappa_{ff}(\nu) + \sigma_T n_e + \sigma_R(\nu) n_1, \quad (47)$$

where $\kappa_{\text{bf}}(\nu)$ and $\kappa_{\text{ff}}(\nu)$ are bound-free and free-free absorption coefficients, respectively. They can be found, for instance, in Mihalas (1978). $\sigma_{\text{T}} = 6.65 \cdot 10^{-25} \text{ cm}^2$ is the Thomson scattering cross section and $\sigma_{\text{R}}(\nu)$ is the Rayleigh scattering cross section evaluated due to approximate formulae by Kurucz (1970). Because the scattering is assumed to be isotropic, the source function S_ν can be written as

$$S_\nu = \frac{\eta_\nu}{\chi_\nu}. \quad (48)$$

The source function S_ν is determined from integration of the system of ordinary differential equations (20)–(24) and is evaluated at each cell center $X_{j-1/2}$ as a function of frequency ν .

Solution of the radiation transfer equation when applied to the radiative shock waves is accompanied by some difficulties. First, because the shock wave propagates in the nearly neutral hydrogen gas, the slab has the appreciably large optical depth in the Lyman continuum ($\tau \sim 10^2$), whereas in the Balmer and higher order continua the total optical depth is very small. For example, the ratio of the total optical depth at the Lyman continuum edge to that in the Balmer continuum is as high as $\sim 10^6$. Thus, in order to obtain the stable solution for the entire frequency range we have to treat the transfer equation as a two-point boundary value problem. Second, the optical depth increments

$$\Delta\tau_{vj} = \frac{1}{2} (\omega_{\nu_{j-1/2}} \Delta m_{j-1/2} + \omega_{\nu_{j+1/2}} \Delta m_{j+1/2}), \quad (49)$$

are extremely small for hydrogen continua of order $i \geq 3$. Here $\omega_\nu = \chi_\nu/\rho$ and $\Delta m_{j-1/2} = \rho_{j-1/2} \Delta X_{j-1/2}$ is the column mass contained in the cell. The straightforward application of the Feautrier method fails because of the limited machine accuracy. To alleviate this obstacle we employ an improved Feautrier solution proposed by Rybicki & Hummer (1991) and providing with much better numerical conditioning of the recurrence elimination scheme.

Thus, the transfer equation (46) is transformed (see, for example, Mihalas 1978) into the second-order differential equation

$$\mu^2 \frac{d^2 u_{\mu\nu}}{d\tau_\nu} = u_{\mu\nu} - S_\nu, \quad (50)$$

where $u_{\mu\nu}$ is a mean-intensity-like variable defined by

$$u_{\mu\nu} = \frac{1}{2} [I(\mu, \nu) + I(-\mu, \nu)], \quad (51)$$

and μ changes in the range $0 \leq \mu \leq 1$.

The transfer equation (50) is subject to boundary conditions at both surfaces of the slab. Assuming that radiation is produced only by the shock wave and that there is no incoming radiation from external sources, we have

$$\begin{aligned} I_\nu(\mu) &= 0 & \text{for } X = X_1, \\ I_\nu(-\mu) &= 0 & \text{for } X = X_N, \end{aligned} \quad (52)$$

The boundary conditions (52) are used in the second-order accuracy Taylor's expansion of the mean-intensity-like variable

u_ν at both boundaries of the slab and are sufficient to complete the system of the finite-difference transfer equations.

The transfer equation (50) is solved each cycle of global iterations for mean-intensity-like variable $u_{\mu\nu}$ defined at the cell centers. The total number of cells is $500 \leq N \leq 1200$ depending on the shock wave model. The frequency range $\nu_B \leq \nu \leq \nu_A$ is divided into N_C intervals, where the upper boundary of the range is $\nu_A = 10^{16} \text{ Hz}$. Boundaries of the intervals correspond to the threshold ionization frequencies and the lower boundary of the frequency range ν_B is the ionization threshold frequency of the N_C -th bound state. Within each interval the integral with respect to frequency ν is replaced by the Gaussian quadrature sum, so that the integral over the whole frequency range $[\nu_B, \nu_A]$ is obtained by summation of interval integrals. The angular range $0 \leq \mu \leq 1$ is also replaced by a set of angular points $\{\mu_i\}$ at the Gaussian quadrature nodes. In the present study the number of quadrature nodes within each frequency interval and the number of angular points were $N_Q = N_m = 4$. Integrating u_ν with respect to μ and ν we evaluated in each cell center the mean intensity J_ν , the radiation energy density E_{rad} , the radiation pressure Pr and the divergence of radiative flux $\nabla \cdot \mathbf{F}_r$. The total radiative flux was calculated in cell boundaries from

$$F_r = 4\pi \int_0^\infty \int_0^1 v_{\mu\nu} \mu d\mu d\nu, \quad (53)$$

where

$$v_{\mu\nu} = \frac{1}{2} [I(\mu, \nu) - I(-\mu, \nu)] = \mu \frac{du_{\mu\nu}}{d\tau_\nu} \quad (54)$$

is an antisymmetric flux-like variable. It should be noted that according to our conventions the radiative flux is negative if the radiation propagates in negative direction. Thus, the radiative flux emerging ahead the discontinuous jump is always negative.

5. The global iteration procedure

For integration of the system of ordinary differential equations (20)–(24) we have to know the mean intensity J_ν and the divergence of radiation flux $\nabla \cdot \mathbf{F}_r$ at each cell center of the shock wave model. On the other hand, the radiation transfer equation (50) can be solved only when the extinction and emission coefficients are given in each cell center. In order to take into account a coupling between gas material and radiation field we employ the iteration procedure. If the initial approximation is enough close to the final solution, we may hope that each iteration will give a better approximation for the final solution than the previous one. In Fig. 1 is shown the flow chart where the main steps of the global iteration procedure are depicted.

Within the whole shock wave both the radiation field and atomic level populations are in a strong departure from LTE. This feature is the principal difficulty accompanying the shock wave model calculations because it is responsible for the narrow convergence area of global iterations. In particular, the use of the initial LTE approximation allows the converged solution to

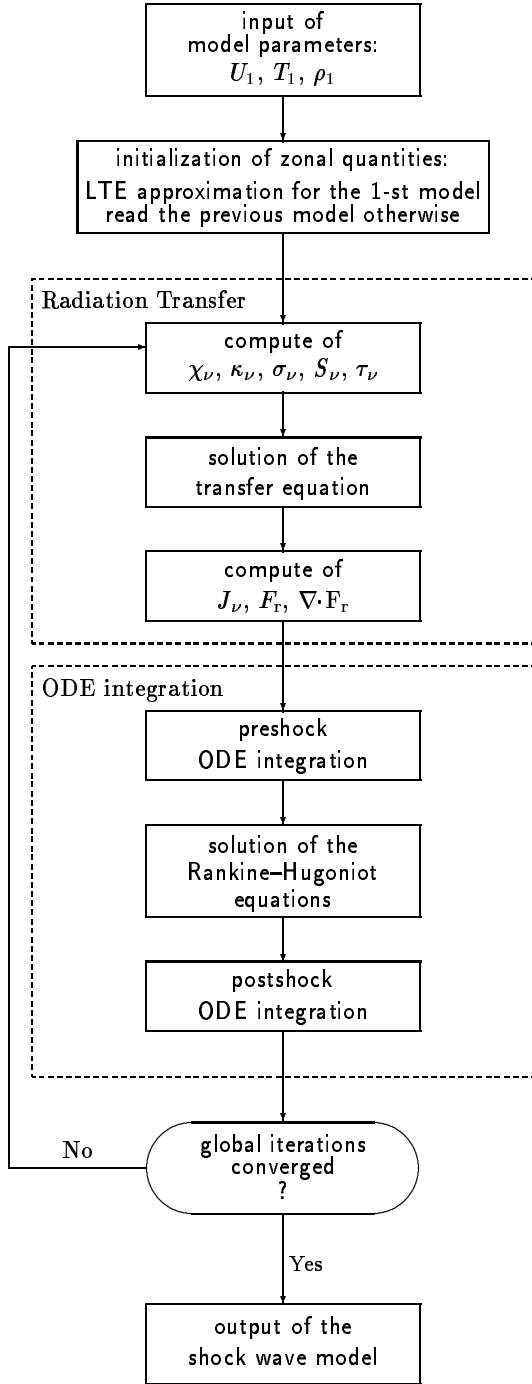


Fig. 1. The flow chart of the global iteration procedure

be obtained only for the weak shock waves with upstream Mach numbers $M_1 \lesssim 3$. For larger upstream velocities the initial oscillation amplitude of the solution vector \mathbf{Y} becomes so large that some quantities fall beyond their physical meaning. In order to alleviate this difficulty and to be able to consider the structure of stronger shock waves we computed a grid of the shock wave models with gradually increasing upstream Mach number, the LTE initial approximation being used only for the first model with the Mach number $M_1 = 2.3$. Thus, each model of the grid

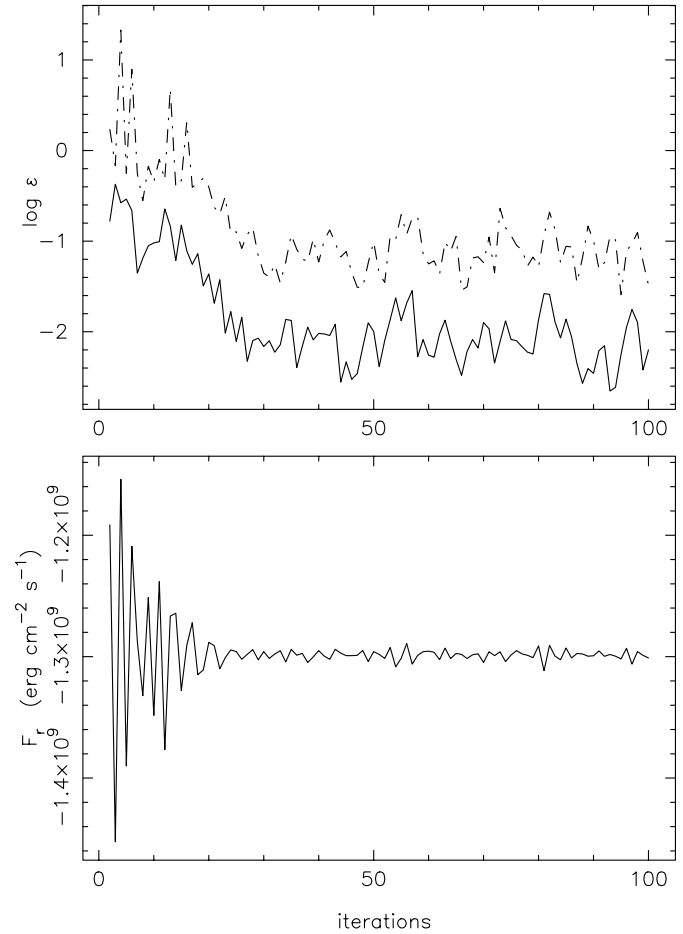


Fig. 2. Upper panel: convergence plots for the electron temperature (solid line) and the divergence of radiative flux (dot-dashed line) given by the maximum absolute relative change ϵ . Lower panel: convergence plot for the total radiative flux emerging from the outer boundary of the preshock region

with exception of the first one was computed with initial approximation obtained from the previous converged model having somewhat smaller upstream velocity. The upstream velocity increment was in the range $1 \text{ Km s}^{-1} \leq \Delta U_1 \leq 5 \text{ Km s}^{-1}$. For test purposes some models were computed with different initial conditions taken from shock wave models with both larger and smaller upstream velocities. In all such cases the shock wave structure was found to converge to a single solution.

In order to describe the convergence of global iterations we introduce for each component of the solution vector \mathbf{Y} at the ℓ -th iteration the quantity

$$\epsilon = \max_{1 \leq j \leq N} \left| 1 - \frac{y_j^{\ell-1}}{y_j^\ell} \right|$$

specifying the maximum absolute relative change of the variable y across the whole shock wave model. A typical behaviour of global iterations is shown in Fig. 2 displaying in the upper panel the maximum absolute relative change of the electron temperature and the divergence of radiative flux within the whole shock wave model. On the lower panel of Fig. 2 is shown the iterative

change of the total radiative flux F_r emerging ahead the shock wave. Thus, if the initial approximation is good enough, we obtained in all cell centers of the model the exponentially decaying oscillations of the solution vector. The global iterations were stopped when relative changes of variables ceased to decrease. The final relative changes of the solution vector depend on the both spatial resolution of the discrete model and accuracy of integration of differential equations (20) – (24). It should be noted also that the convergence of global iterations appreciably varies for different regions of the shock wave. In particular, the convergence is best in the radiative precursor and thermalization zone, whereas in the recombination zone becomes slower. Thus, the convergence plots shown in Fig. 2 display mostly variations of the solution vector in the vicinity of the outer boundary of the postshock region.

6. Results of calculations

In this paper we discuss the results of calculations done for the shock waves with upstream velocities $15 \text{ Km s}^{-1} \leq U_1 \leq 60 \text{ Km s}^{-1}$ propagating through the unperturbed hydrogen gas of temperature $T_1 = 3000 \text{ K}$ and density $\rho_1 = 10^{-10} \text{ gm cm}^{-3}$ ($n_H = 6.02 \cdot 10^{13} \text{ cm}^{-3}$). In total we computed 46 models with upstream velocity increment of $\Delta U_1 = 1 \text{ Km s}^{-1}$. The outer boundary of the preshock region, where the gas is assumed to be unperturbed, is set at $X \approx -9.2 \cdot 10^5 \text{ cm}$. Calculations were done for the two-level hydrogen atom, the first atomic state being treated in non-LTE. The radiation transfer equation was solved for the both Lyman and Balmer continua ($N_C = 2$). Thus, the frequency point nearest to the Lyman edge frequency $\nu_{01} = 3.288 \cdot 10^{15} \text{ Hz}$ was set at $\nu_{01} = 3.754 \cdot 10^{15} \text{ Hz}$. More extensive calculations for the larger number of bound atomic states L and hydrogen continua N_C as well as for various temperatures T_1 and densities ρ_1 of the unperturbed gas will be given in the forthcoming paper.

The most fascinating feature of radiative shock waves is that they demonstrate the strong interaction between gas material flows and the radiation field which they produce. This interplay is best seen from the plots of the divergence of radiative flux as a function of the spatial coordinate X . One of such plots is shown in Fig. 3. By definition, the divergence of radiative flux is negative, if the fluid absorbs more energy than emits and, therefore, is heated. And conversely, when $\nabla \cdot \mathbf{F}_r > 0$, the gas radiatively cools since it radiates more energy than it absorbs.

As is seen in Fig. 3, the divergence of radiative flux is always negative in the preshock zone, the departure of $\nabla \cdot \mathbf{F}_r$ from zero gradually increasing while the gas approaches the discontinuous jump. Heating of the precursor gas material is due to absorption of the Lyman continuum radiation, hence the region, where the divergence of radiative flux $\nabla \cdot \mathbf{F}_r$ perceptibly deviates from zero, extends over a few units of the optical depth at frequency ν_{01} .

The properties of the radiation field do not change appreciably across the discontinuous jump. The spatial resolution of our shock wave models near the discontinuous jump is limited by the space interval $X_J - X_{J-1/2} = 0.5 \text{ cm}$. The change of F_r

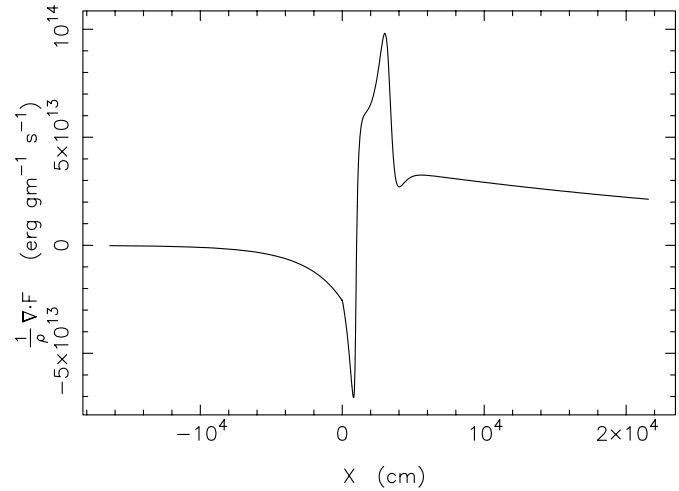


Fig. 3. The divergence of radiative flux against the spatial coordinate in the shock wave model with $U_1 = 40 \text{ Km s}^{-1}$

and $\nabla \cdot \mathbf{F}_r$ over this interval increases with increasing upstream velocity U_1 but does not exceed 0.3% for $U_1 = 60 \text{ Km s}^{-1}$. Thus, just behind the discontinuous jump the divergence of radiative flux goes on to gradually decrease and reaches the minimum in the vicinity of the maximum of the electron temperature T_e . The rapid growth of the divergence of radiative flux behind its minimum implies that the gas material flows into the radiatively cooling zone. For the shock wave model with $U_1 = 40 \text{ Km s}^{-1}$ the distance between maximum and minimum of $\nabla \cdot \mathbf{F}_r$ is $\approx 2.2 \cdot 10^3 \text{ cm}$ and corresponds to the optical depth between these layers of $\tau(\nu_{01}) \approx 3.5$. It should be noted that both the minimum and maximum of the divergence of radiative flux as well as other properties of the shock wave very strongly (for some variables nearly exponentially) depend on the upstream velocity U_1 .

6.1. The radiative precursor

At the outer boundary of the preshock region the first level of the hydrogen atom is approximately in LTE since the Lyman continuum radiation emerging from the postshock region is negligible. Both the Saha-Boltzmann relation and equations of statistical equilibrium give nearly the same (within a few per cent) the hydrogen ionization degree of $x_H \sim 10^{-8}$. The main sources of opacity are bound-free transitions in the Lyman continuum (i.e. at frequencies $\nu \geq \nu_{01} = 3.288 \cdot 10^{15} \text{ Hz}$) and at lower frequencies the Rayleigh scattering by hydrogen atoms in the ground state. The free-free opacity and the Thomson scattering are negligible. With approaching to the discontinuous jump the hydrogen ionization degree increases, so that the both free-free opacity and Thomson scattering increase but nevertheless even for $U_1 = 60 \text{ Km s}^{-1}$ they remain negligible within the entire preshock region.

The radiative precursor is revealed as the part of the preshock region where the hydrogen gas is heated and is ionized by the Lyman continuum radiation emerging from the postshock region. The temperature of heavy particles (neutral hydrogen atoms and

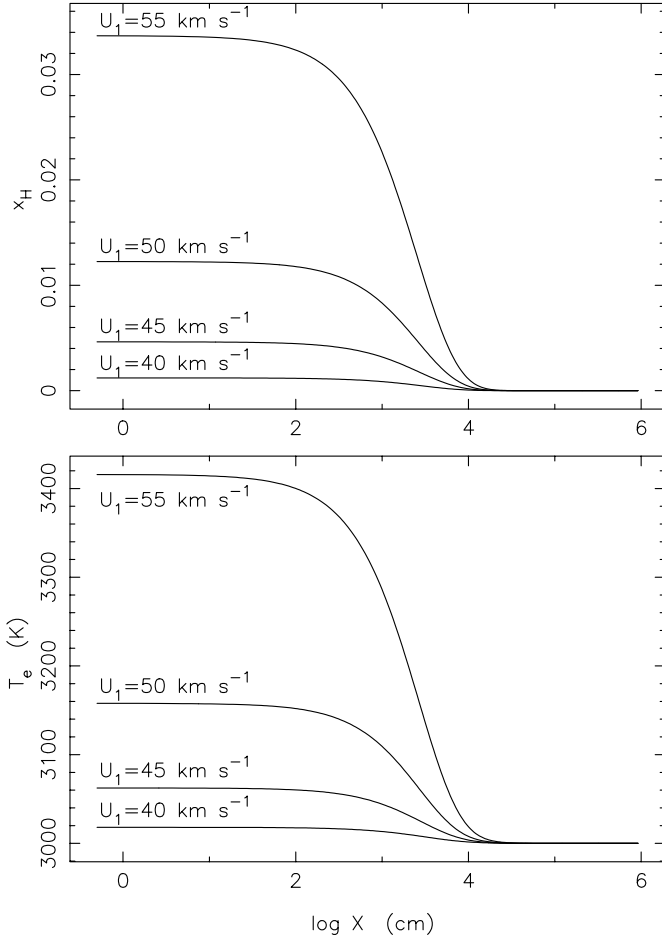


Fig. 4. The hydrogen ionization degree x_H (upper panel) and the electron temperature T_e (lower panel) in the preshock region of the shock wave models with upstream velocities $U_1 = 40, 45, 50$ and 55 Km s^{-1}

hydrogen ions) T_a remains constant ($T_a = T_1 = 3000\text{K}$) in the radiative precursor. In Fig. 4 are shown the plots of the electron temperature T_e and the hydrogen ionization degree x_H as a function of the distance from the discontinuous jump for the shock wave models with upstream velocities $U_1 = 40, 45, 50$ and 55 Km s^{-1} . As is seen, the perceptible heating and ionization occur at distances from the discontinuous jump smaller than $X_{\text{prec}} \approx 3 \cdot 10^4 \text{ cm}$. The distance X_{prec} corresponds to the optical depth of $\tau(\nu_{01}) \sim 3$. Thus, for $U_1 \leq 60 \text{ Km s}^{-1}$ the geometrical thickness of the radiative precursor approximately does not depend on the upstream velocity.

Within the radiative precursor the hydrogen gas and radiation field are in strong departure from LTE. In particular, ionization of hydrogen atoms is mainly due to radiative transitions, whereas collisional recombinations appreciably exceed collisional ionizations. Fig. 5 shows the rates of radiative transitions R_{1k} and $R_{k1} = (n_1^*/n_e^*)R_{1k}^\dagger$ as well as the collisional rates $n_e C_{1k}$ and $n_e C_{k1} = n_e(n_1^*/n_e^*)C_{1k}$ as a function of X for the shock wave model with $U_1 = 40 \text{ Km s}^{-1}$. The precursor transition rates are very sensitive to the upstream velocity U_1 . For example, for upstream velocities $20 \text{ Km s}^{-1} \leq U_1 \leq 60 \text{ Km s}^{-1}$

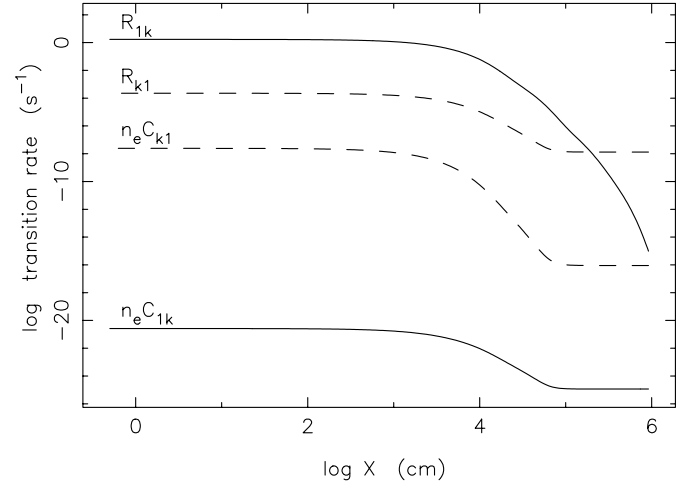


Fig. 5. The rates of ionizations (solid lines) and recombinations (dashed lines) against the distance from the discontinuous jump in the preshock region of the shock wave model with $U_1 = 40 \text{ Km s}^{-1}$

the rates of ionizations from the ground state increase in the ranges $-7.1 \leq \log R_{1k} \leq 2.6$ and $-25.8 \leq \log(n_e C_{1k}) \leq -10.6$, respectively. However, notwithstanding such a strong dependence on U_1 , for all shock wave models the spatial dependencies of transition rates were found to be qualitatively similar to those displayed in Fig. 5.

The growth of the hydrogen ionization degree with approaching to the discontinuous jump is accompanied by the increase of the gas pressure gradient. The corresponding decrease of the gas material velocity becomes, however, perceptible only for $U > 50 \text{ Km s}^{-1}$. For example, at the inner boundary of the preshock region the relative decrease of U is $\approx 0.15\%$ for $U_1 = 55 \text{ Km s}^{-1}$ and is $\approx 0.5\%$ for $U_1 = 60 \text{ Km s}^{-1}$.

Of great interest are the physical conditions at the inner boundary of the preshock region. For the models considered in the present study the spatial coordinate of this boundary is $X_{J-1/2} = -0.5 \text{ cm}$. For upstream velocities $U_1 \lesssim 28 \text{ Km s}^{-1}$ both the hydrogen ionization degree and the electron temperature nearly do not change within the preshock region. These quantities show the perceptible dependence on upstream velocity only for $U_1 > 28 \text{ Km s}^{-1}$. In Table 1 we give the hydrogen ionization degree x_H , the electron temperature T_e as well as the transition rates at the inner boundary of the preshock region. For the sake of convenience the upstream velocity U_1 is given in Km s^{-1} .

The electron temperature just ahead the discontinuous jump increases with increasing upstream velocity nearly exponentially. For the shock wave models of the present study this dependence can be approximately expressed due to the following fitting formula

$$\log T_e = 3.303 + 2.115 \cdot 10^{-2} U_1 - 7.590 \cdot 10^{-4} U_1^2 + 8.326 \cdot 10^{-6} U_1^3, \quad (55)$$

where the upstream velocity U_1 is expressed, for the sake of convenience, in Km s^{-1} .

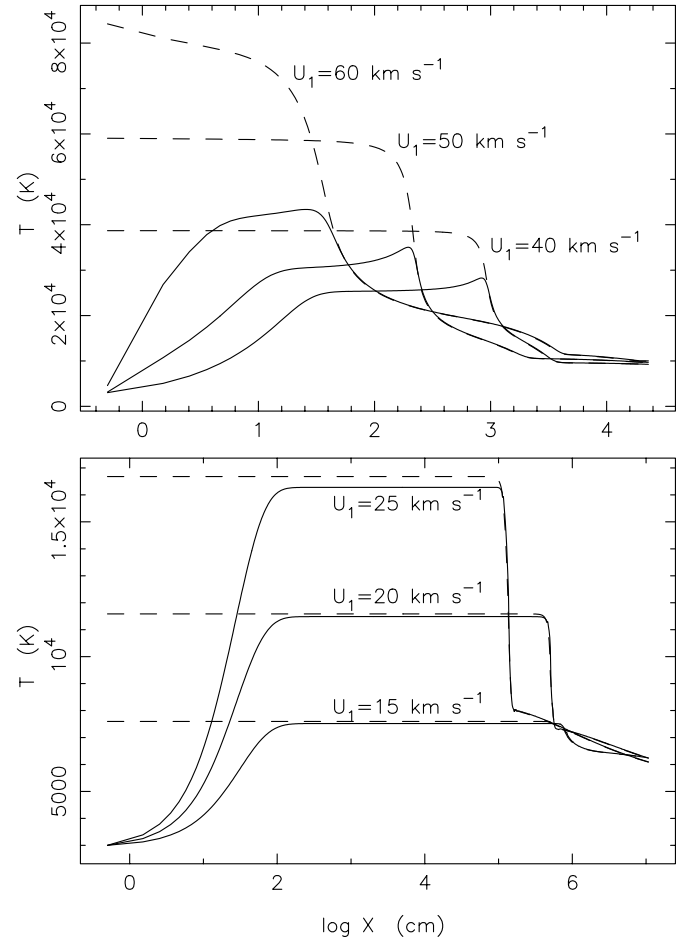
Table 1. The properties of the preshock inner boundary

U_1	$\log x_H$	T_e	\log (transition rate s^{-1})			
			R_{1k}	R_{k1}	$n_e C_{1k}$	$n_e C_{k1}$
15	-8.04	3000	-7.36	-8.79	-25.85	-17.86
20	-8.04	3000	-7.11	-8.79	-25.85	-17.86
25	-8.04	3000	-7.01	-8.79	-25.85	-17.86
30	-7.21	3000	-4.86	-7.99	-25.05	-16.26
35	-4.19	3002	-1.20	-4.93	-21.98	-10.16
40	-2.92	3018	0.23	-3.65	-20.58	-7.61
45	-2.33	3062	0.90	-3.03	-19.67	-6.45
50	-1.91	3158	1.40	-2.53	-18.56	-5.62
55	-1.47	3416	1.90	-1.91	-16.46	-4.77
60	-0.84	4590	2.63	-0.75	-10.61	-3.62

As is seen in Table 1, the dominating process just ahead the discontinuous jump is photoionization and, therefore, the shortest relaxation time in the radiative precursor is that of photoionizations from the ground state $t_{\text{phi}} = 1/R_{1k}$. The photoionization relaxation time gradually decreases with increasing upstream velocity from $t_{\text{phi}} \approx 2 \cdot 10^7$ s for $U_1 = 15 \text{ Km s}^{-1}$ to $t_{\text{phi}} \approx 2 \cdot 10^{-3}$ s for $U_1 = 60 \text{ Km s}^{-1}$. Comparing these relaxation times with the time needed for gas to flow through the precursor $t_{\text{hyd}} = X_{\text{prec}}/U_1$ we find that for models with upstream velocities $U_1 < 50 \text{ Km s}^{-1}$ the ratio of the photoionization relaxation time to the hydrodynamic time is $t_{\text{phi}}/t_{\text{hyd}} \gg 1$ and only for $U_1 = 60 \text{ Km s}^{-1}$ the photoionization relaxation time becomes nearly comparable with hydrodynamic time: $t_{\text{phi}}/t_{\text{hyd}} \approx 0.4$. Because for establishment of the statistical equilibrium this ratio should be $t_{\text{phi}}/t_{\text{hyd}} \ll 1$, the ground state populations of the hydrogen atom are in strong departure from the statistical equilibrium and the hydrogen ionization degree cannot be described in assumption of statistical equilibrium. For example, at the inner boundary of the preshock region of the shock wave model with $U_1 = 50 \text{ Km s}^{-1}$ the hydrogen ionization degree is $x_H = 1.22 \cdot 10^{-2}$, whereas solution of the equations of statistical equilibrium gives $x_H = 0.99$.

6.2. The thermalization and recombination zones

Behind the discontinuous jump the translational kinetic energy of heavy particles is redistributed among various degrees of freedom characterized by different relaxation times. The fastest relaxation process is the translational kinetic energy exchange in elastic collisions of electrons with neutral atoms and ions. Another relaxation process is excitation of bound atomic states and ionization of hydrogen atoms. Both excitation and ionization need, however, much more collisions than translational kinetic energy exchange (Stupochenko et al. 1967), so that just behind the discontinuous jump the electron temperature gradually increases, whereas the hydrogen ionization degree remains nearly constant. Note that although the bound-bound transitions were not considered in our model, the excitation of atomic states is taken into account as a result of bound-free transitions.

**Fig. 6.** The electron temperature T_e (solid lines) and temperature of heavy particles T_a (dashed lines) as a function of distance from the discontinuous jump in the postshock region

In Fig. 6 are shown the electron temperature T_e and the temperature of heavy particles T_a as a function of distance from the discontinuous jump for shock wave models with upstream velocities from 15 Km s^{-1} to 60 Km s^{-1} . As is seen, the characteristic time of the electron temperature growth rapidly decreases with increasing upstream velocity. Furthermore, for $U_1 < 30 \text{ Km s}^{-1}$ there is a temperature plateau within of which both temperatures approximately do not change until they begin to decrease. The existence of the temperature plateau is due to the fact that for upstream velocities $U_1 < 30 \text{ Km s}^{-1}$ the electrons acquire the energy from heavy particles due to elastic collisions with neutral hydrogen atoms. The rate of energy gain in such collisions is very small and gradually decreases when the electron temperature T_e approaches the temperature of heavy particles T_a . The temperature plateau appears when the electron energy gain in elastic collisions with neutral hydrogen atoms becomes almost negligible. At upstream velocities $U_1 > 30 \text{ Km s}^{-1}$ the electron temperature plateau is ended by the slight bump, the bump being wider and higher with increasing U_1 .

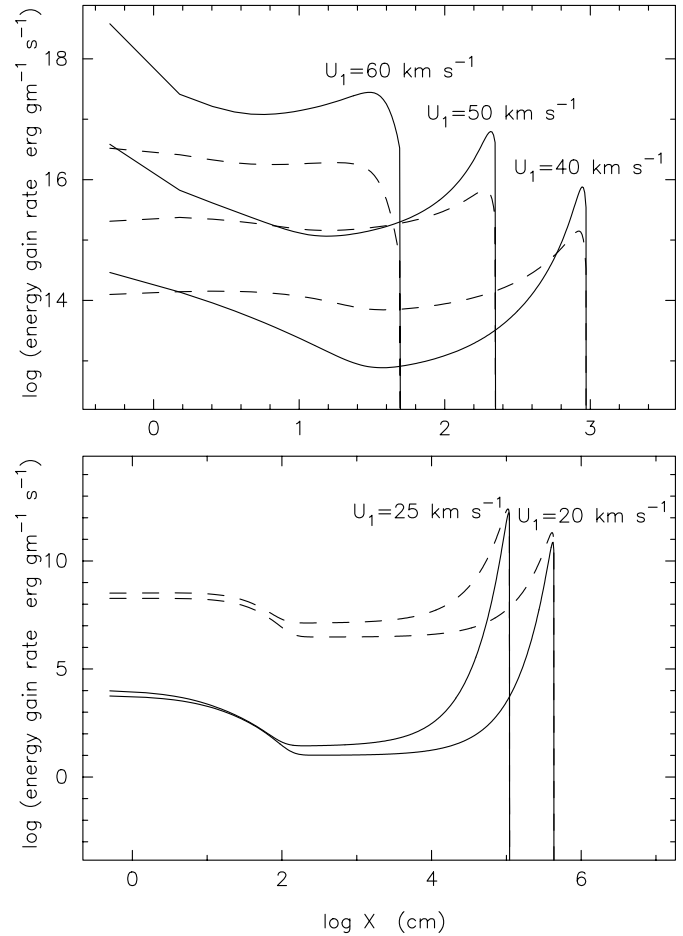
Table 2. Properties of the postshock region

U_1	T_e	$\log X$	x_H	$\log X$	$\log \nabla \cdot \mathbf{F}_r$	$\log \frac{F_{ly}}{F_r}$
15	7521		0.014	6.29	11.097	-5.22
20	11486		0.071	5.72	12.671	-3.43
25	16281	4.95	0.134	5.16	13.201	-2.83
30	20986	4.20	0.206	4.40	13.473	-2.80
35	24712	3.42	0.294	3.89	13.749	-2.19
40	28274	2.92	0.406	3.61	13.992	-1.81
45	31681	2.58	0.528	3.43	14.198	-1.66
50	35050	2.29	0.662	3.32	14.381	-1.49
55	38575	1.96	0.805	3.22	14.569	-1.23
60	43371	1.40	0.964	2.89	14.848	-0.74

In the second and third columns of Table 2 are given both the maximum value of the electron temperature in the postshock region as well as the distance of this point from the discontinuous jump expressed in cm. In the first column of Table 2 we give the upstream velocity expressed, for the sake of convenience, in Km s^{-1} . The electron temperature peak was not found for the shock wave models with $U_1 \leq 20 \text{ Km s}^{-1}$ and in these cases we give only the electron temperature of the plateau. The electron temperature maximum can be approximately considered as a point where temperatures of heavy particles and free electrons equilibrate. Thus, the width of the relaxation zone where both temperatures equalize decreases by a factor of ≈ 3600 for the upstream velocity increasing from 25 Km s^{-1} to 60 Km s^{-1} . It is of interest to note that for upstream velocities $U_1 < 50 \text{ Km s}^{-1}$ the temperature of heavy particles T_a remains nearly constant until the electron temperature begins to increase just before its drop. This is due to the fact that at small upstream velocities the fractional abundance of free electrons is so small that they cannot perceptibly affect the gas of heavy particles.

The translational energy exchange between heavy particles and electrons is due to elastic collisions of electrons with both neutral hydrogen atoms and hydrogen ions. The cross section of elastic collisions with hydrogen ions is much larger than that of electrons with neutral atoms and, therefore, the translational energy gain by electrons from heavy particles is strongly dependent on the hydrogen ionization degree. The rates of energy gain by electrons in both these processes are shown in Fig. 7. The abrupt decrease of Q_{ei} and Q_{ea} occurs when both temperatures equalize.

For shock wave models considered in the present study the rate of energy gain by electrons in elastic collisions with ions exceeds that in elastic collisions with neutral atoms only when the hydrogen ionization degree is $x_H \gtrsim 10^{-2}$. As is seen in Fig. 7, for upstream velocities $U_1 \leq 25 \text{ Km s}^{-1}$, the electron temperature equalizes with temperature of heavy particles only due to elastic collisions of electrons with neutral atoms. Comparing with lower panel of Fig. 6 one sees that when the electron temperature reaches the plateau, the rate of energy gain Q_{ea} decreases by nearly two orders of magnitude.

**Fig. 7.** The rates of energy gain by electrons in elastic collisions with hydrogen ions (solid lines) and neutral hydrogen atoms (dashed lines)

At upstream velocities $30 \text{ Km s}^{-1} < U_1 < 50 \text{ Km s}^{-1}$, the energy gain in elastic collisions with ions begins to dominate only just before the temperature drop. It is this increase of Q_{ei} that is responsible for the electron temperature peak near the end of the electron temperature plateau. The translational energy gain by electrons in elastic collisions with hydrogen ions becomes completely dominating for $U_1 > 50 \text{ Km s}^{-1}$. The gradual decrease of Q_{ei} just behind the discontinuous jump in the shock wave models with $U_1 \geq 40 \text{ Km s}^{-1}$ (see upper panel of Fig. 7) is due to the temperature dependence of the equipartition time given in Eq. (34).

In Fig. 8 are shown the plots of the hydrogen ionization degree in the postshock region of the shock wave models with upstream velocities $U_1 = 40, 50$ and 60 Km s^{-1} . Comparing with Fig. 6 one sees that the maximum of the hydrogen ionization occurs at much larger distances from the discontinuous jump than the maximum of the electron temperature. Very approximately the distances of both these maxima can be expressed as power functions of the upstream velocity:

$$X(\max T_e) = 1.21 \cdot 10^9 U_1^{-6.96}, \quad (56)$$

$$X(\max x_H) = 6.07 \cdot 10^7 U_1^{-5.60}. \quad (57)$$

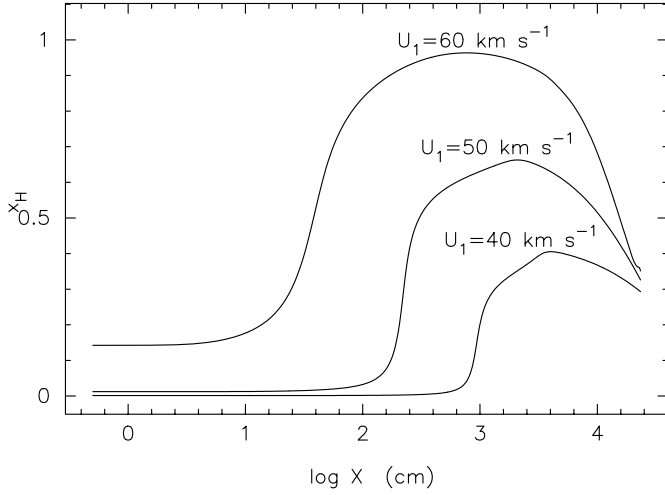


Fig. 8. The hydrogen ionization degree as a function of the distance from the discontinuous jump in the shock wave models with upstream velocities $U_1 = 40, 50$ and 60 Km s^{-1}

In these approximate expressions, for the sake of convenience, the distances $X(\max T_e)$ and $X(\max x_H)$ are expressed in km whereas the upstream velocity is expressed in Km s^{-1} . The maximum values of x_H as well as the corresponding distances from the discontinuous jump expressed in cm are given in the fourth and fifth columns of Table 2, respectively. According to the schematical division of the shock wave noted above the maximum of x_H can be considered as the boundary between the thermalization and recombination zones.

The large distance between maxima of the electron temperature and the hydrogen ionization degree implies that the degree of freedom associated with ionization of hydrogen atoms is frozen in comparison with excitation of translational motions. As a result, the gas flows through the maximum of T_e at smaller heat capacity C_p than it would be in equilibrium. Thus, when the perceptible fraction of hydrogen atoms is ionized, the gas density begins to increase. At larger distances the gas density goes on to increase due to the radiative cooling (see Fig. 9).

The total ionization rate of hydrogen atoms is a sum of photoionizations and collisional ionizations, so that it depends on the number density of free electrons. Because no ionization occurs across the discontinuous jump, the total ionization rate behind the discontinuous jump strongly depends on the ionization in the radiative precursor. To demonstrate this dependence, in Fig. 10 are shown the rates of ionizations and recombinations, both collisional and radiative, in the postshock regions of the shock waves with upstream velocities 30 and 50 Km s^{-1} .

For the shock wave model with $U_1 = 30 \text{ Km s}^{-1}$ the hydrogen ionization degree at the discontinuous jump is $x_H \approx 6 \cdot 10^{-8}$, therefore just behind the discontinuous jump the role of collisional ionizations is negligible and the number density of free electrons increases initially only due to photoionizations. For $U_1 = 50 \text{ Km s}^{-1}$ the hydrogen ionization degree at the discontinuous jump is $x_H \approx 10^{-2}$. Free electrons created in the precursor play a role of the seeds producing yet more electrons and leading to the electron avalanche.

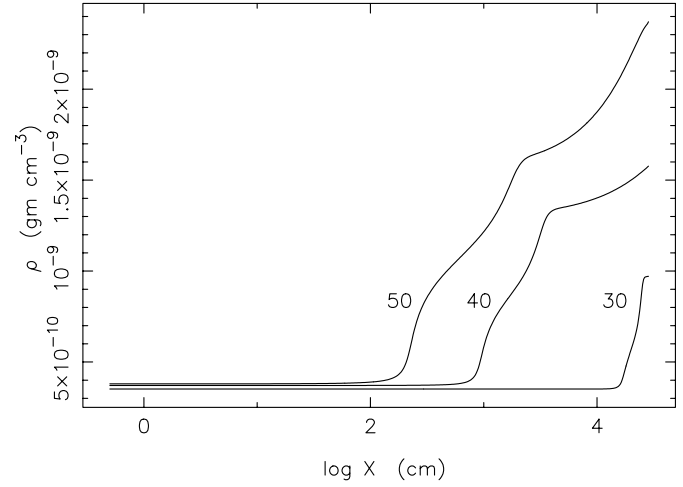


Fig. 9. The postshock gas density ρ against the distance from the discontinuous jump. The numbers at the curves indicate the upstream velocity U_1 in Km s^{-1}

Compared to the preshock region where the contribution of opacity sources nearly does not depend on the upstream velocity, the gradual growth of the hydrogen ionization degree behind the discontinuous jump leads to the appreciable dependence of postshock opacities on the upstream velocity U_1 . For $U_1 < 30 \text{ Km s}^{-1}$ the postshock opacity in the Balmer continuum is mainly due to Rayleigh scattering by neutral hydrogen atoms. Only near the Balmer edge, the opacity due to bound-free transitions from the second level becomes most important. With increasing upstream velocity the role of the bound-free transitions from the second level increases and for $U_1 > 50 \text{ Km s}^{-1}$ this opacity mechanism becomes dominating within the whole range of the Balmer continuum. The role of the Thomson scattering is somewhat perceptible only near the Balmer edge, whereas the free-free opacity can be neglected.

6.3. The radiation field

Although we did not include into the system of ordinary differential equations (20) – (24) the terms with radiation energy density E_{rad} and radiation pressure P_r , these quantities were evaluated as

$$E_{\text{rad}} = \frac{4\pi}{c} \int_0^\infty \int_0^1 u_{\mu\nu} d\mu d\nu \quad (58)$$

$$P_r = \frac{4\pi}{c} \int_0^\infty \int_0^1 u_{\mu\nu} \mu^2 d\mu d\nu \quad (59)$$

together with total radiative flux F_r and divergence of the radiative flux $\nabla \cdot \mathbf{F}_r$ each time when the radiation transfer equation was solved. For the fixed spatial coordinate X the ratio of the radiation energy density to the total translational kinetic energy gradually increases with increasing upstream velocity and is in the range $5 \cdot 10^{-4} \lesssim E_{\text{rad}}/(E_a + E_e) \lesssim 0.02$ for

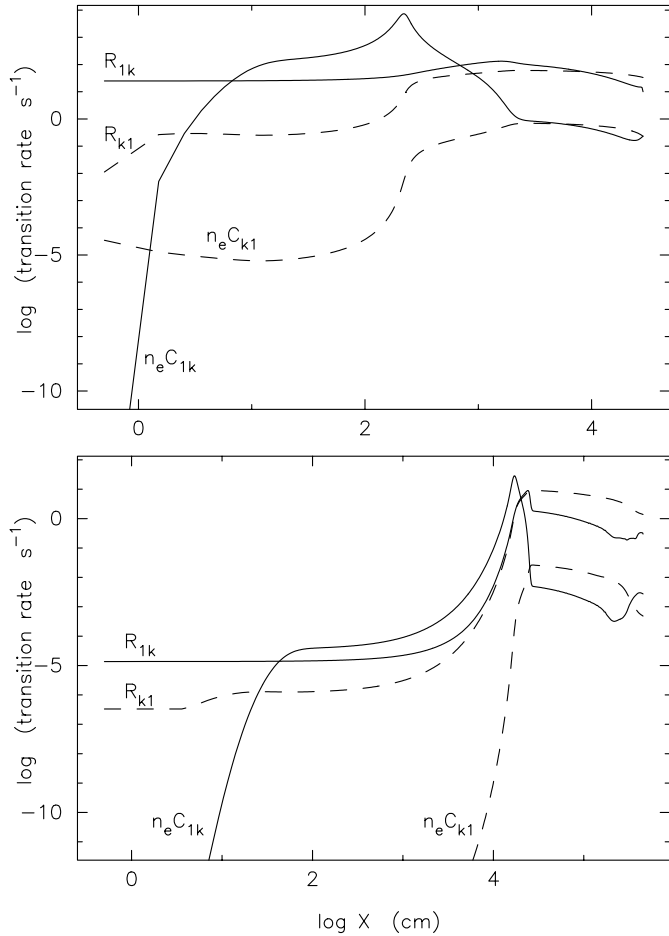


Fig. 10. The rates of ionizations (solid lines) and recombinations (dashed lines) against the distance from the discontinuous jump X in the postshock region. Upper panel: $U_1 = 50 \text{ Km s}^{-1}$; lower panel: $U_1 = 30 \text{ Km s}^{-1}$

$20 \text{ Km s}^{-1} \leq U_1 \leq 60 \text{ Km s}^{-1}$. The ratio $E_{\text{rad}}/(E_a + E_e)$ is highest at the inner boundary of the preshock region because just behind the discontinuous jump the total translational kinetic energy increases by more than an order of magnitude, whereas the total change of E_{rad} within the shock wave does not exceed 30%. Because the most of the energy flux is contained in the radiative flux F_r , we find that $UE_{\text{rad}}/F_r \lesssim 2.3 \cdot 10^{-4}$ for $U_1 = 60 \text{ Km s}^{-1}$. Thus, our assumption that the radiation energy and radiation pressure can be neglected is enough good.

In Fig. 11 are shown the dependencies of E_{rad} on the distance from the discontinuous jump for the both preshock and postshock regions of the model with $U_1 = 60 \text{ Km s}^{-1}$. The increase of E_{rad} in the preshock region with approaching to the discontinuous jump is due to the radiative heating by the layers absorbing the Lyman continuum radiation. Behind the discontinuous jump the radiation energy density reaches the maximum in the hydrogen recombination zone.

The most of the shock wave radiation, by definition, is produced in the layers where the divergence of radiative flux $\nabla \cdot \mathbf{F}_r$ reaches the maximum. These layers locate nearly at the same distance from the discontinuous jump as the maximum of the

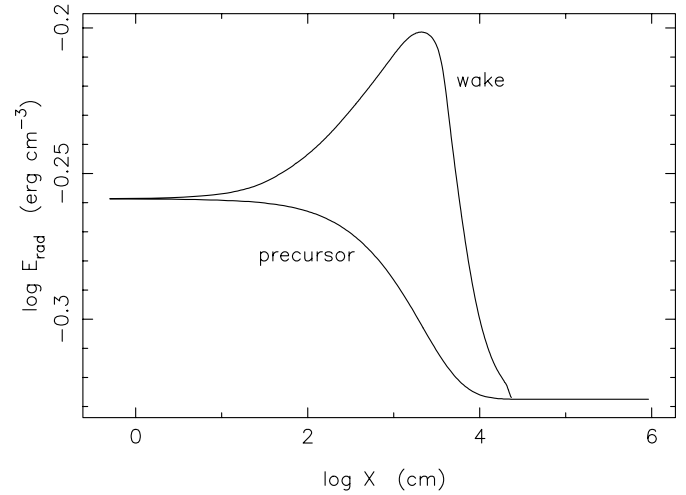


Fig. 11. The total radiation energy density as a function of distance from the discontinuous jump in the shock wave model with $U_1 = 60 \text{ Km s}^{-1}$

hydrogen ionization degree. The maximum of $\nabla \cdot \mathbf{F}_r$ exponentially increases with increasing upstream velocity and for $20 \text{ Km s}^{-1} \leq U_1 \leq 60 \text{ Km s}^{-1}$ is given by

$$(\nabla \cdot \mathbf{F}_r)_{\text{max}} = 1.25 \cdot 10^{12} \exp(0.105U_1) \text{ erg gm}^{-1}\text{s}^{-1}, \quad (60)$$

where the upstream velocity is expressed in Km s^{-1} . Maximum values of $\nabla \cdot \mathbf{F}_r$ are given in the sixth column of Table 2.

As was noted above the shock wave models have a small optical depth in the Balmer continuum ($\tau_{\text{max}} \sim 10^{-4}$) and at the same time they are opaque for the Lyman continuum photons. Therefore, the radiation emerging from the both surfaces of the slab is mostly within the Balmer continuum whereas the Lyman continuum radiation is transported only within the narrow zone surrounding the discontinuous jump. In the lower panel of Fig. 12 for the shock wave model with upstream velocity $U_1 = 40 \text{ Km s}^{-1}$ is shown the Lyman continuum radiative flux F_{Ly} as a function of the spatial coordinate X . This dependence is qualitatively similar to that of the divergence of radiative flux shown in Fig. 3. The negative flux corresponds to the radiation propagating in the direction of the preshock region. The optical depth between minimum and maximum of F_{Ly} is $\Delta\tau(\nu_{01}) \approx 4.4$ for $U_1 = 40 \text{ Km s}^{-1}$ and slowly decreases from $\Delta\tau(\nu_{01}) \approx 24$ for $U_1 = 30 \text{ Km s}^{-1}$ to $\Delta\tau(\nu_{01}) \approx 1$ for $U_1 = 60 \text{ Km s}^{-1}$. This decrease is mostly due to the growth of the hydrogen ionization degree in the postshock region. The ratios of the maximum radiation flux transported within the Lyman continuum to the total radiation flux are given in the last column of Table 2.

In the upper panel of Fig. 12 for the same model is shown the total radiative flux F_r . This plot displays only the very vicinity of the discontinuous jump. In the preshock region, beyond the radiative precursor, the total radiative flux F_r remains constant since the divergence of radiative flux is $\nabla \cdot \mathbf{F}_r = 0$. In the postshock region the total radiative flux gradually increases and asymptotically tends to the same value as in the preshock but with the opposite sign. For all shock wave models we obtained that the total radiative fluxes emerging from both surfaces of the slab are $-F_{r1} = F_{rN}$.

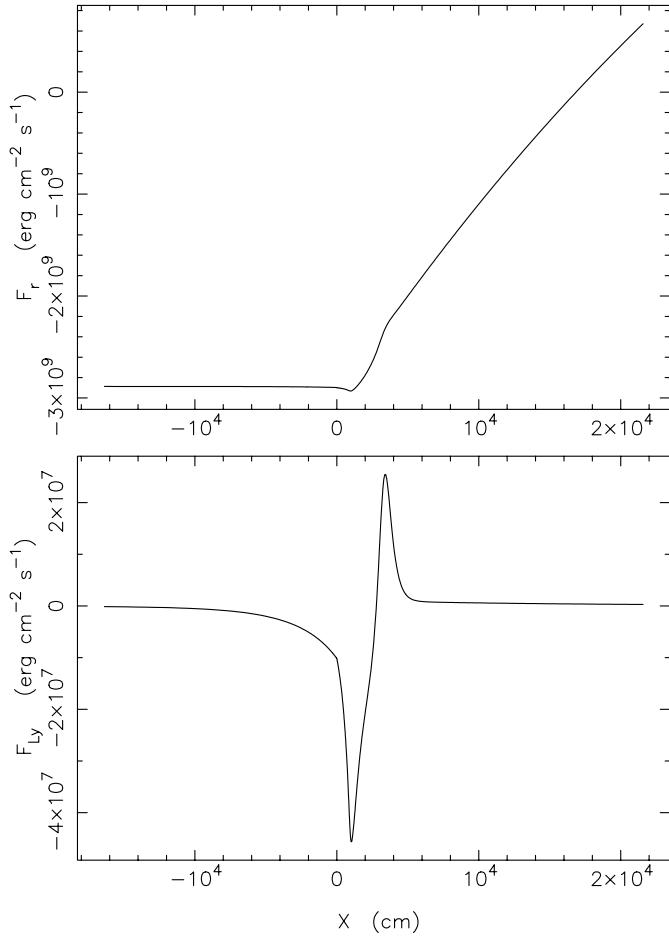


Fig. 12. The radiative flux within the Lyman continuum F_{Ly} (lower panel) and the total radiative flux F_r (upper panel) against the spatial coordinate X for the shock wave model with $U_1 = 40 \text{ Km s}^{-1}$

7. Conclusion

The primary goal of the work reported in this paper was to obtain the self-consistent solution of the equations of fluid dynamics, rate equations and radiation transfer equation for the structure of the steady shock wave. The procedure of global iterations described in the present paper in general resembles the compute of stellar atmosphere models. Indeed, like in stellar atmosphere calculations the shock wave model takes into account the coupling between the gas material and radiation field. The self-consistent model is obtained with iteration procedure comprising the solution of the radiation transfer equation and integration of the mass, momentum and energy conservation equations written in the form of the ordinary differential equations. Each cycle of iterations gives, in general, improved characteristics of the gas and radiation field.

At the same time, the problem of the shock wave structure compared to that of stellar atmosphere models contains a number of serious complications. First, atomic level populations are not only in strong departures from LTE but are also in significant departures from statistical equilibrium. Second, unlike the stellar atmospheres, where the divergence of radia-

tive flux is $\nabla \cdot \mathbf{F}_r = 0$ (the condition of radiative equilibrium), in shock waves the part of the energy of hydrodynamic flow is transformed into radiation and the radiative equilibrium is established only far away from the discontinuous jump. Furthermore, in stellar atmosphere models the total radiative flux is given as one of the boundary conditions, whereas in the shock wave model the emerging flux is obtained from the solution of the problem. The small optical depth increments in hydrogen continua of order $l \geq 3$ lead to the losses of the machine accuracy when the Feautrier technique is applied. The problem is so serious, that even the improved method by Rybicki & Hummer (1991) sometimes fails. Third, the rate equations are stiff and need the special treatment in their solution. In particular, the convergence of global iterations depends on the tolerance parameter determining the maximum error permitted during the integration.

The present paper is confined by consideration of the two-level atomic model, so that the radiation transfer is treated for the Lyman and Balmer continua, only. This approximation seems to be insufficient for the shock wave problem because the occupation numbers of levels $l \geq 2$ obviously deviate from LTE and the perceptible fraction of radiation is transported at frequencies lower than the Balmer edge frequency. Nevertheless, notwithstanding such a restriction, there is a qualitative agreement of our results with those obtained earlier by other authors. For example, according to calculations of Gillet & Lafon (1990) the electron temperature just ahead the discontinuous jump is $T_e \approx 14000\text{K}$ for the upstream velocity of $U_1 = 80 \text{ Km s}^{-1}$. Although in the present study the highest upstream velocity was $U_1 = 60 \text{ Km s}^{-1}$, a very approximate comparison can be done with fitting formula (55) which gives the same electron temperature for the upstream velocity $U_1 \approx 75 \text{ Km s}^{-1}$. Thus, more detailed calculations are needed and in the forthcoming paper we are going to present the grid of the shock wave models computed for the larger number of hydrogen atomic levels and wider range of upstream velocities, the models of the present study being used as initial approximation for more correct shock wave models.

More realistic models, however, should take into account not only bound-free terms but also bound-bound terms in the rate equations and the radiation transfer problem should be solved for the both continuum and spectral line radiation. This is the perspective for the near future. It is certainly one of the most basic. Indeed, preceding shock studies show that radiative processes, which determine the wake cooling, have a strong influence on the resulting shock structure. Because in the model of this paper we consider a pure H-plasma without H^- , and only include the bound-free photo- and collisional processes of H atoms, we expect that the absence of some predominant coolants such as neutral and singly ionized metal atoms might appreciably underestimate the radiative cooling rate of the gas. The importance of radiative heating and cooling rates in shocked circumstellar envelopes have been recently investigated (Woitke et al. 1996) but only a few transitions of the numerous metal lines were considered. At present such a basic study seems to be beyond our immediate abilities and is out of the scope of

our paper which was to investigate the possibility of obtaining a self-consistent solution of the structure of radiative shock waves in dense atmospheric gas.

Acknowledgements. The authors are indebted to the referee, Dr. Peter Woitke, for his meticulous review of this paper and for his valuable comments. The work of YAF has been done in part under the auspices of the Ministère de l'Enseignement Supérieur et de la Recherche (grant 1196/MDLM/CB) in 1996 and of the Aix-Marseille I University (grant 34 PR 1049) in 1997. YAF acknowledges also the support from the Russian Foundation for Basic Research (grant 95-02-06359).

References

- Clarke, J.H., Ferrari, C., 1965, *Phys. Fluid*, 8, 2121
 Farnsworth, A.V., Clarke, J.H., 1971, *Phys. Fluid*, 14, 1352
 Foley, W.H., Clarke, J.H., 1973, *Phys. Fluid*, 16, 375
 Gillet, D., Lafon J.-P.J., 1984, *A&A*, 139, 401
 Gillet, D., Lafon J.-P.J., David, P., 1989, *A&A*, 220, 185
 Gillet, D., Lafon J.-P.J., 1990, *A&A*, 235, 255
 Hill, S.J., 1972, *ApJ*, 178, 793
 Hindmarsh, A.C., 1979, LLNL Report, Nb. Ucl-82091
 Klein, R.I., Stein, R.F., Kalkofen, W., 1976, *ApJ*, 205, 499
 Klein, R.I., Stein, R.F., Kalkofen, W., 1978, *ApJ*, 220, 1024
 Kogure, T., 1962, *PASJ*, 14, 247
 Kurucz, R.L., 1970, SAO Special Report, Nb. 309
 Liberman, M.A., Velikovich, A.L., *Physics of Shock Waves in Gases and Plasmas*, 1986, Springer, Heidelberg
 Mihalas, D., 1967, *ApJ*, 149, 169
 Mihalas, D., *Stellar Atmospheres*, 1978, Freeman, San Francisco
 Mihalas, D., Mihalas, B.W., *Foundations of Radiation Hydrodynamics*, 1984, Oxford University Press, Oxford
 Murty, S.S.R., 1971, *J. Quant. Spectrosc. Radiat. Transfer*, 11, 1681
 Narita, S., 1973, *Prog. Theor. Phys.*, 49, 1911
 Nelson, H.F., Goulard R., 1968, *Phys. Fluid*, 12, 1605
 Nelson, H.F., 1973, *Phys. Fluid*, 16, 2132
 Rybicki, G.B., Hummer, D.G. 1991, *A&A*, 245, 171
 Sachdev, P.L., 1968, *PASJ*, 20, 264
 Skalafuris, A., 1968, *J. Quant. Spectrosc. Radiat. Transfer*, 8, 515
 Spitzer, L., Härm, R., 1953, *Phys. Rev.*, 89, 977
 Stupochenko, Ye.V., Losev A.V., Osipov A.I., *Relaxation in Shock Waves*, 1967, Springer, New York
 Whitney, C.A., Skalafuris, A.J., 1963, *ApJ*, 138, 200
 Woitke, P., Krüger, D., Sedlmayr, E., 1996, *A&A*, 311, 927
 Zel'dovich, Ya.B., Raizer, Yu.P., *Physics of Shock Waves and High-Temperature Hydrodynamic Phenomena*, 1966, Academic Press, New York